Asian Journal of Chemistry; Vol. 35, No. 6 (2023), 1500-1508

ASIAN JOURNAL OF CHEMISTRY

https://doi.org/10.14233/ajchem.2023.27877

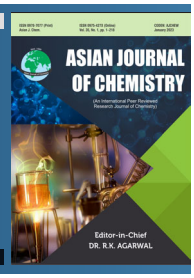

Photocatalytic Degradation of Crystal Violet Dye in Aqueous Solution using $ZnFe_2O_4$-Cellulose Nanocomposite Catalyst

ALKA SINGH[1], N.B. SINGH[1,2] and RICHA TOMAR[1,*]

[1]Department of Chemistry and Biochemistry, Sharda University, Plot no. 32, 34, Knowledge Park III, Greater Noida-201310, India
[2]Research Development Centre, Sharda University, Greater Noida-201310, India

*Corresponding author: E-mail: richa.tomar@sharda.ac.in

Received: 6 April 2023; *Accepted*: 8 May 2023; *Published online*: 27 May 2023; AJC-21269

The major issue in the modern area is the wastewater discharge, particularly the organic pigments from several industries, which creates various pernicious health hazards. As a result, synthesized zinc ferrites and cellulose nanocomposites are effective photocatalysts used for the detoxification of crystal violet dyes. The crystallite-size of synthesized zinc ferrite nanoparticle was confirmed from XRD by using Scherrer equation to be 25.5 nm. The elemental composition of the zinc ferrite-cellulose nanocomposite was clearly shown by the EDS spectrum. Based on the FESEM micrographs, the zinc ferrite-cellulose nanocomposite morphology revealed a smooth surface with microspheres measuring 500 nm in size. The $ZnFe_2O_4$-cellulose nanocomposite demonstrated 92% photocatalytic efficiency for the removal of crystal violet dye at pH 6 after 160 min of sunlight irradiation with a catalyst dosage of 50 mg and an initial dye concentration of 10 ppm. The pseudo-second-order kinetic model was found to be consistent for the photocatalytic process. Finally, the newly developed photocatalyst ($ZnFe_2O_4$-cellulose nanocomposites) should be considered better for dye decontamination in wastewater.

Keywords: Photocatalyst, Zinc ferrite-cellulose nanocomposite, Adsorption, Crystal violet dye.

INTRODUCTION

Water pollution is one of the major problem faced by the entire world as a result of rapid industrialization. Different dye are used in textile industries, including pulp mills, cosmetics, printing, pharmaceuticals, paper and food, to improve their compositional qualities [1]. These fields create a significant quantity of coloured wastewater production, which is released as untreated wastewater, causing water pollution [2].

Dyes are extremely resistant to biodegradation processes, yet their toxicity is harmful to both human and aquatic health. Colouring cotton, silk and wood, among other things, is one of the most common uses of dyes [3]. The health problems of crystal violet dye include burns to the eyes in both animals and humans, difficulties in breathing, vomiting, sweating, kidney, reproductive, jaundice, mutations, an increase in heartbeat, cancer and damage to the brain and central nervous system [4]. Therefore, for the removal of crystal violet dye, a convenient procedure is needed. Flocculation, coagulation, biological oxidation, degradation, sedimentation, photocatalytic oxidation, membrane processes, electrochemical oxidation, *etc.* are different technologies used for the removal of harmful organic dyes from the aqueous solution [5].

One of the most eco-friendly processes is photocatalysis for the removal of dyes from wastewater from industries [6]. Metal oxides are a fascinating research area for scientists; they are used as semiconductors due to their catalytic, optical and electronic properties. For the removal of harmful organic dyes, numerous photocatalysts in the form of semiconductors have been created and analyzed [7]. However, because of their wide bandgap, these semiconductors have a problem. The bandgap in the visible range of a photocatalyst have to be as narrow as possible. Upon valence band to conduction band photoelectron excitation, a redox process on the semiconductor surface results in the removal of dyes [8].

For a long time, ferrites were regarded as an effective material for the elimination of pollutants among the different heterogeneous catalysts due to several qualities like intense activity, large surface area, high ratio of surface to volume, simple synthetic technique and simple recovery [9]. However,

the problem of agglomeration is a major disadvantage of using ferrites as a catalyst. Ferrites agglomerate due to their inherent magnetic properties, reducing their dispersibility, stability and thus catalytic properties [10]. As a result, aggregation must be avoided to expose their absolutely amazing qualities. To stabilize these ferrite nanoparticles, intermediates made of carbon nanotubes, polyethylene, cellulose and pectin were utilized [11].

Because of the growing concern about the environment and the effects of industrial processes, the demand is expanding for alternative methods of utilizing the natural resources. Biomass derived cellulose as an eco-friendly and sustainable material [12]. The ferrite nanoparticles are stabilized using cellulose as a template. Cellulose nanofibers have attracted a lot of attention for their synthesis and usage in composite materials due to their distinctive features, such as a high surface-to-volume ratio, an extensive surface area, superior mechanical capabilities and sizes at the nanoscale [13]. The current study focuses on the photocatalytic degradation of the pollutant crystal violet dye using cellulose-based nanocomposites [14].

EXPERIMENTAL

Ferric chloride ($FeCl_3$, Fisher-Scientific, Germany) with purity 99.99%, crystal violet dye, sodium hydroxide, zinc chloride, cellulose powder (from wood pulp) supplied by Byhut, Jaipur, India.

Preparation of cellulose: Cellulose powder (1 g) was mixed into a 20% NaOH solution for 3 h at room temperature. Then after filtration the activated cellulose ($C_6H_{10}O_5$*NaOH) was collected.

Synthesis of zinc ferrite/cellulose nanocomposites: In 100 mL of deionized water, dissolved stoichiometric amounts of $FeCl_3$ (0.6 g) and $ZnCl_2$ (1 g). After that gradually 0.2 M of NaOH solution was added to the mixture to maintain pH 12. The yellowish-brown precipitate is formed. At 60 ºC, 1 g of active cellulose was added to the yellowish-brown powder and stirred vigorously for 3 h. After centrifuging, distilled water and ethanol were used to wash the composite twice and then dried at 60 ºC for 48 h.

Characterization: Different techniques were used to characterize the prepared zinc ferrite-cellulose nanocomposites and cellulose, including FTIR using wavenumbers ranging from 4000 to 500 cm^{-1}, UV-1800 double-beam spectrophotometer, the FESEM and EDX (by EVO MA15/18 and 51N1000-EDS System, respectively with maximum resolution of 512 nm) from the Centre for Nanoscience and Nanotechnology, Jamia Millia Islamia, New Delhi, India. SEM has been used to study the surface morphology. The X-ray diffraction (XRD) helps in the study of crystal phase and purity of zinc ferrite-cellulose nanocomposite by X-ray diffractometer using Cu$K\alpha$ radiation, which was recorded between the 2θ values of 10-60º.

Photocatalytic studies: Organic crystal violet dye was used to investigate the catalytic characteristics of zinc ferrite-cellulose nanocomposite. A photocatalytic removal procedure was carried out using 20 mg to 50 mg dose of catalyst, 2-10 ppm dye concentration under pH 2-10 at 30-60 ºC at noon for 160 min with the constant stirring in the presence of solar light irradiation to attain the stability of adsorption and desorption between the catalyst and the crystal violet dye. The UV/VIS double-beam spectrophotometer was used to take the absorbance of solution. The following expression was used to calculate the percentage (%) of removal as follows [15]:

$$\text{Removal (\%)} = \frac{A_0 - A}{A_0} \times 100 \quad (1)$$

where A_0 = initial absorbance, A = absorbance of dye solution.

RESULTS AND DISCUSSION

UV-visible studies: The prepared $ZnFe_2O_4$-cellulose nanocomposite was investigated by UV/visible spectra at the range of 200-800 nm. The absorption edge of ferrite is legitimated in the visible region to the excitation of electrons from O-2*p* to Fe-3*d* state which is spinel type pragmatic nanoparticles [16] (Fig. 1). The absorbance peak of $ZnFe_2O_4$-cellulose nanocomposite is at 472 nm.

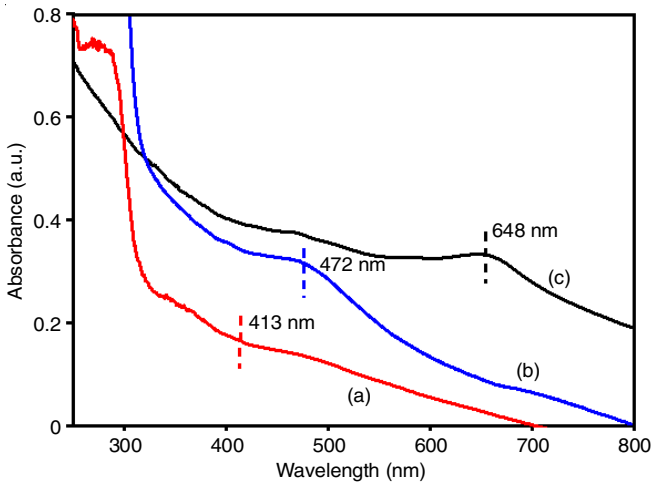

Fig. 1. UV-visible spectra of (a) $ZnFe_2O_4$ nanoparticles, (b) $ZnFe_2O_4$-cellulose nanocomposites, (c) cellulose

Tauc plot is used to determine the optical band gap of $ZnFe_2O_4$-cellulose nanocomposite based on eqn. 2 [17].

$$(\alpha h\nu) = A\,(h\nu - Ev)^n \quad (2)$$

where α = absorption coefficient, A = constant, Ev = the energy gap, n = an index used to characterize the optical absorption process and hν = the energy of incident photon [18].

The tauc polts of $(\alpha h\nu)^2$ against hν (eV) of $ZnFe_2O_4$-cellulose nanocomposite is depicted in Fig. 2. The band gap energy was observed to be 1.8 eV, which is well within the range of the recorded values [19]. The optimal band gap necessary for optical applications as photocatalysts is quite near to this band gap value.

FTIR studies: The compared FTIR spectra of $ZnFe_2O_4$ nanoparticles, cellulose and prepared $ZnFe_2O_4$-cellulose nanocomposite is presented in Fig. 3. The observed peaks were at 3371.13, 1659.4, 1156.03, 1044.2 and 656.4 cm^{-1}. A stretching vibration at 3371.13 cm^{-1} in the spectrum of $ZnFe_2O_4$-cellulose nanocomposite is due to C–H stretching which shows an alkane group is present. A peak at 1659.4 cm^{-1} is attributed due to the

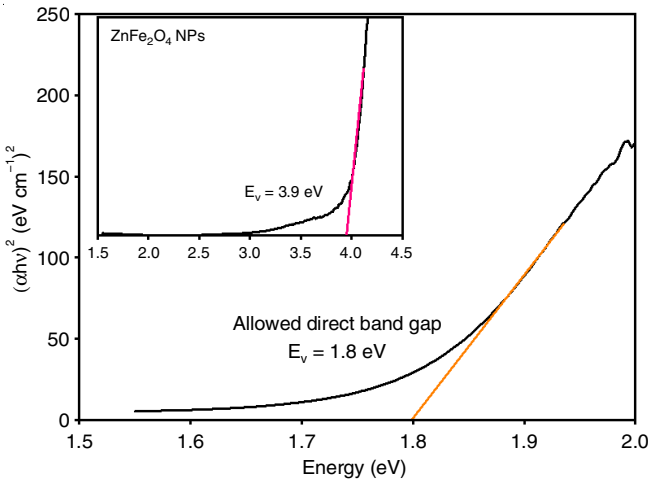

Fig. 2. Tauc plot of $ZnFe_2O_4$-cellulose nanocomposites

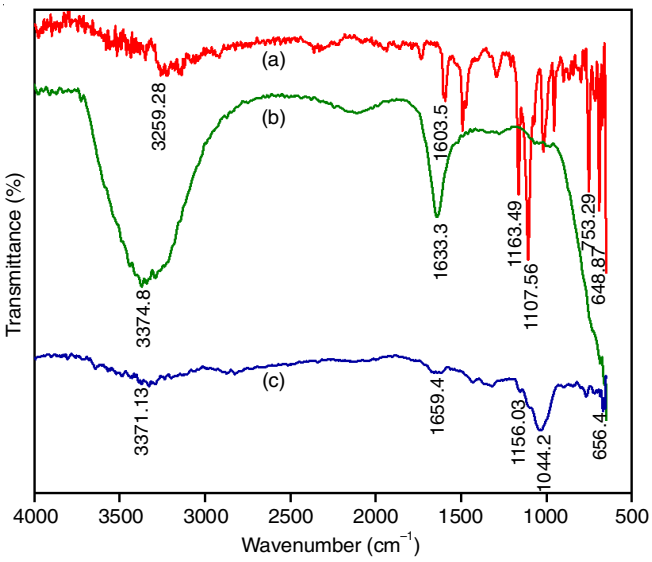

Fig. 3. FTIR spectral analysis of (a) $ZnFe_2O_4$ NPs, (b) cellulose, (c) $ZnFe_2O_4$-cellulose NCs

C=C stretching. The peak at 1156.03 cm^{-1}. The peak at 1156.03 cm^{-1} shows the bending of the C–H and O–H group. The peak at 1044.2 cm^{-1} indicates C–O and C–N stretching band which shows the presence of secondary alcohol and aromatic amine, respectively [20]. The weak bands at 656.4 cm^{-1} assigned to the Fe–O and Zn–O vibrations represent the tetrahedral and octahedral modes of $ZnFe_2O$, respectively [16]. The presence of these distinct peaks demonstrated a strong interaction between spinel $ZnFe_2O_4$ and the cellulose matrix [21].

XRD studies: A powdered XRD pattern of $ZnFe_2O_4$-cellulose nanocomposites in Fig. 4 shows their diffraction peaks that are distinct from cellulose. The $ZnFe_2O_4$ diffraction peaks were found at 2θ values of 20.5º, 30.2º, 34.8º, 37.9º, 45.4º, 55.6º and 62.4º, which correspond to the reflection patterns of (111), (220), (311), (222), (400), (422) and (511), respectively showing the presence of spinel cubic structure [16]. The crystallite size of particles was calculated by using the Scherrer equation (eqn. 3) [22]:

$$D = \frac{K\lambda}{\beta\cos\theta} \quad (3)$$

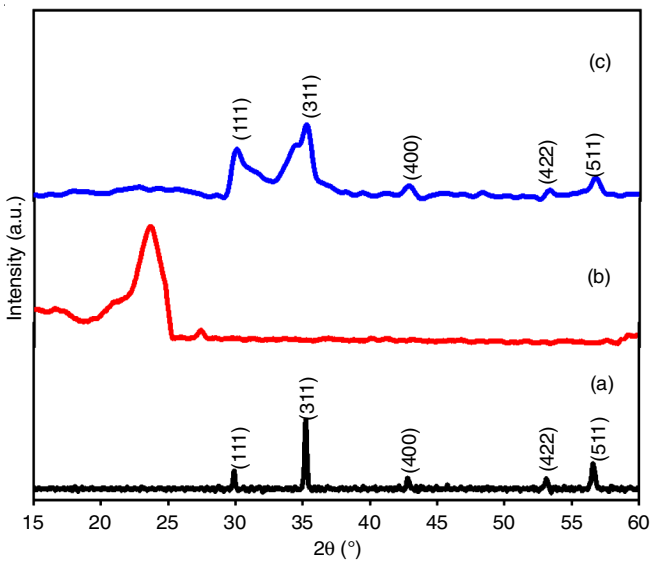

Fig. 4. XRD pattern of powdered (a) $ZnFe_2O_4$ NPs, (b) cellulose, (c) $ZnFe_2O_4$-cellulose nanocomposites

where D = size of crystal in nm, β = the half-width in radian of peak, λ = wavelength (0.154 nm) and θ = diffraction angle.

From eqn. 3, the average crystallite size of $ZnFe_2O_4$ nanoparticles resulted is 25.5 nm. The black line represents a typical pattern of zinc ferrite (Fig. 4a). The crystalline structure of $ZnFe_2O_4$-cellulose nanocomposites materials inherited the same ferrite covering with no discernible alteration in the pattern of zinc ferrite. This could be seen in the blue line pattern (Fig. 4c), which maintained the reflection plane of zinc ferrite without any signs of the cellulose's amorphous nature and the red line pattern (Fig. 4b) shows the sharp peak, at 2θ = 22.6° which indicates the amorphous nature of cellulose.

FE-SEM and EDX studies: The morphological image of cellulose and its ferrite composite can be obtained by field-emission scanning electron microscopy (FE-SEM). From Fig. 5, it is clearly seen that the composite surface was made up of gaps and cylindrical aggregates of homogenous $ZnFe_2O_4$ nanosheets that were dispersed throughout the cellulose fibers, indicating the high porosity of materials. The normal long cellulose fiber are cellulose particles while their composite particles have undergone significant degradation. The hydrogen bonds that connect the cellulose chains intermolecularly is broken by adding zinc ferrite to fibers of the cellulose matrix [23]. Furthermore, the EDX spectra shows peaks linked to the elements, which indicated that the prepared nanocomposite is composed of Zn, Fe, O and C and no any foreign elements was found.

Photocatalysis of crystal violet dye: The efficient removal of crystal violet dye was observed in solar light irradiation by $ZnFe_2O_4$-cellulose nanocomposites. The maximum removal efficiency that affects the photocatalysis process was optimized at different parameters.

Effect of time: From Fig. 6a, it is observed that as the solar light irradiation period increases, the photocatalytic degradation of crystal violet increases. The radiation of visible light has an ability to excite the electrons on exposure with time from lower to higher energy levels. The electromagnetic

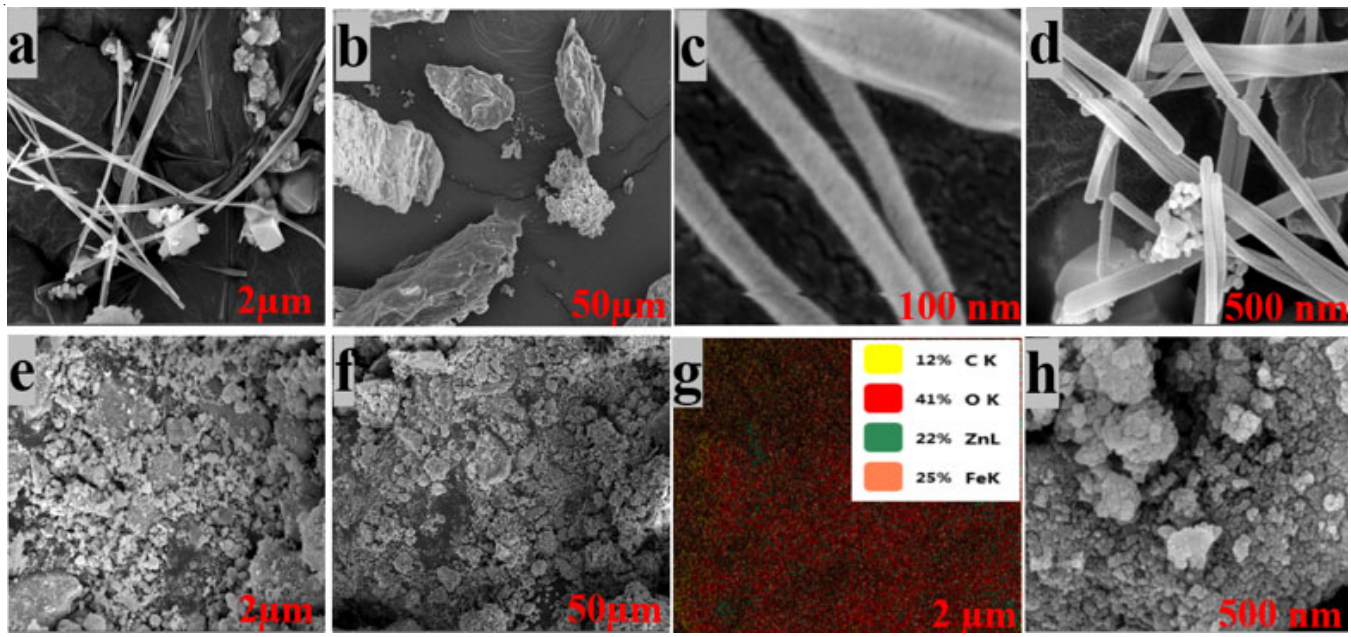

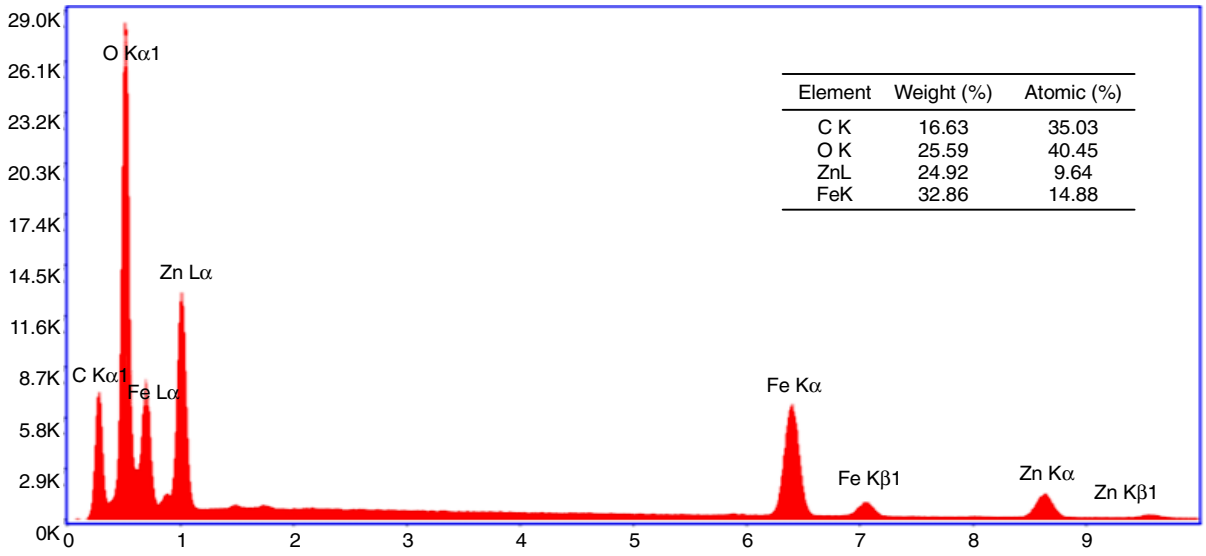

Element	Weight (%)	Atomic (%)
C K	16.63	35.03
O K	25.59	40.45
ZnL	24.92	9.64
FeK	32.86	14.88

Fig. 5. FESEM image of cellulose (a-d) and $ZnFe_2O_4$-cellulose NCs (e-h) and EDX

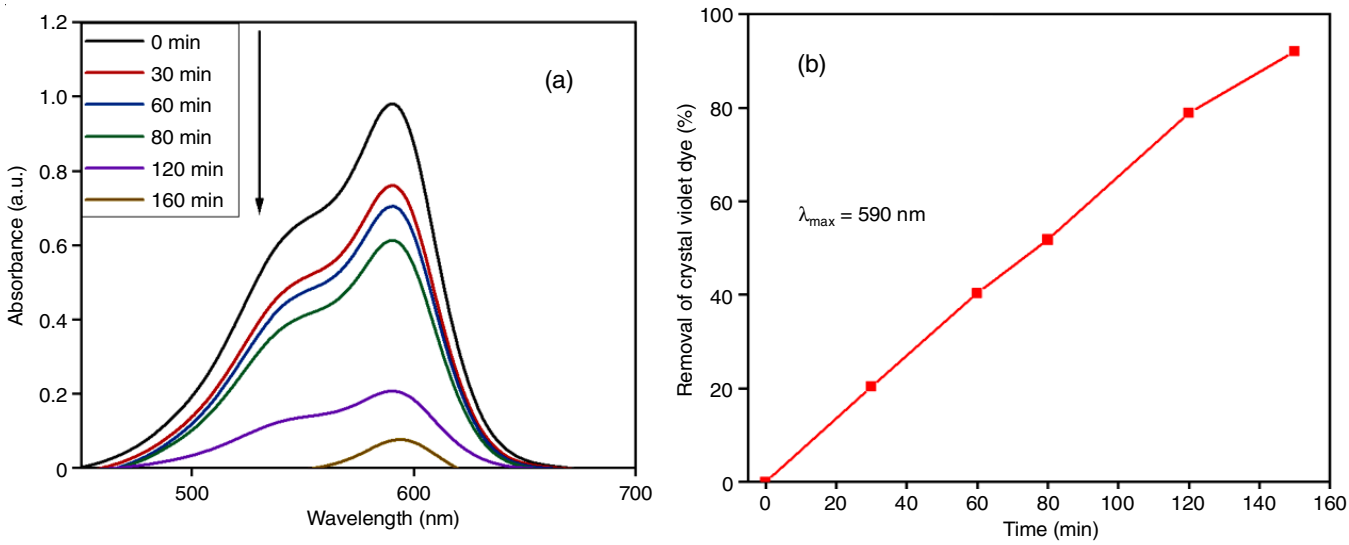

Fig. 6. Effect of time on the removal of crystal violet dye

radiation absorbs energy when radiated on photocatalyst and creates holes in the valence band of the photocatalyst by exciting electron to higher energy. The electron reduces the oxygen to convert it into superoxide and peroxides if the electrons are strong levels of energy from excitement and hydroxyl radicals are formed when the created holes cause the water to oxidize. The removal percentage of dye as shown in Fig. 6b, was high because holes and electrons were readily available at sorption sites on the catalyst surface. As crystal violet dye accumulates over time, it begins to form repellent interactions with molecules in solution and on the surface, the breakdown slows down. Therefore, the crystal violet dye begins to get removed as soon as it was exposed to radiation and after 160 min, no more removal was observed. Hence, this period was chosen as the ideal irradiation time for further studies and approx. 92% of removal was accomplished at the ideal irradiation time. Therefore, it is clear that $ZnFe_2O_4$-cellulose nanocomposite acts as a powerful catalyst for the quick photocatalysis of high concentrations of crystal violet dye.

Effect of pH: Fig. 7 clearly shows that the crystal violet dye removal was highly influenced due to pH variation. The amount of photocatalytic removal increased as the pH raised from 2 to 6 and become constant approximately at pH 7 and then decreased as the pH raised above 7. According to Samsami and Mohamadi [24], the pH had an impact on the degree of adsorbate ionization, the concentration of electrostatic repulsion on the functional groups of the adsorbent and the solubility of metal ions. According to Neethu & Choudhury [25], crystal violet dye (CV), a cationic dye, is strongly acidic at low pH. Thus, highest removal (85%) of crystal violet dye at pH 6 is due to an increased electrostatic attraction between charged surface of $ZnFe_2O_4$-cellulose nanocomposites and dye solution.

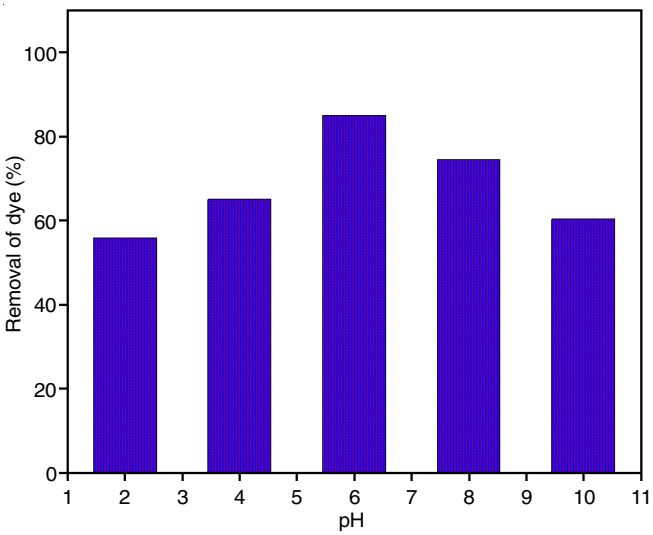

Fig. 7. pH effect on removal percentage of crystal violet dye

Effect of dose: Fig. 8 clearly shows the effect of variation in adsorbent dose on the percentage (%) removal of crystal violet dye with a specified dye concentration of 10 ppm. The absorbance intensity of the dye solution decreases as the amount of dye removed increases with increasing catalyst dose. Maximum dye elimination was achieved at a photocatalyst dose of 50 mg. Thus, the ideal catalyst loading for the removal of crystal violet dye was determined to be 50 mg of $ZnFe_2O_4$-cellulose nanocomposites. The existence of active sites on the surface of absorbent and solar light penetrating to form holes and electrons on the surface of ferrite nanocomposites are responsible for the observed effect. Increasing the catalyst dosage increases the removal rate because more active sites on the catalyst surface become accessible [26].

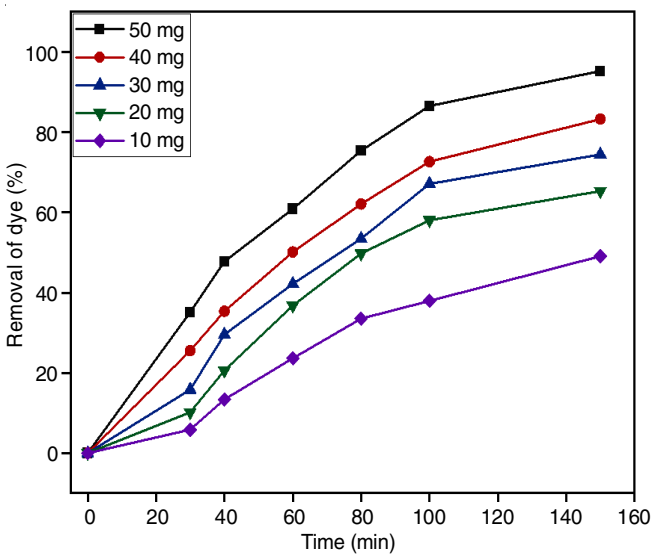

Fig. 8. Effect of adsorbent dose on the percentage of crystal violet dye

Effect of concentration: Fig. 9 shows that different concentrations (2-12 ppm) of dye were used to test the effectiveness of catalyst ($ZnFe_2O_4$-cellulose nanocomposites) on removal of crystal violet dye. The dye adsorbed on the catalyst surface effects the generation of hydroxyl radicals, hence it is observed that the removal is greatly dependent on its concentration [27]. The amount of dye removed, increased as dye concentration raised (2 to 12 ppm) and 92% of dye at 10 ppm was removed due to the highest amount of OH radicals that could be found on the catalyst surface [28]. Further decrease in the concentration removal to 82% may be attributable to the restriction on hole and electron production. As the quantity of dye molecules collected on the catalyst surface increases beyond it, removal decreases [29]. Removal of harmful organic pollutants into a simple byproduct (CO_2, H_2O) is the main purpose of photocatalysis process. In the first step, sunlight was absorbed at a wavelength equivalent to the semiconductor bandgap. The hole formed on the semiconductor area is caused by the absorbed energy moving electrons from the valence band to the conduction band [26]. Superoxide ($O_2^{\bullet-}$) is produced when the oxygen in solution traps an electron in the conduction band (e^-_{CB}). The $OH^\bullet$ radicals are formed when the holes produced during the process interact with the ^-OH group of water molecules. Proton neutralizes the superoxide ($O_2^{\bullet-}$) species. After that, oxygen was temporarily transformed into H_2O_2. Then, the transient decomposition of H_2O_2 resulted from the oxygen reduction. The organic dye represented by R in the mechanism shown below was oxidized by the hydroxyl radicals ($^\bullet OH$) into simple molecules. The oxidative potential holes (h^+_{VB}) directly oxidize the organic dye in this process.

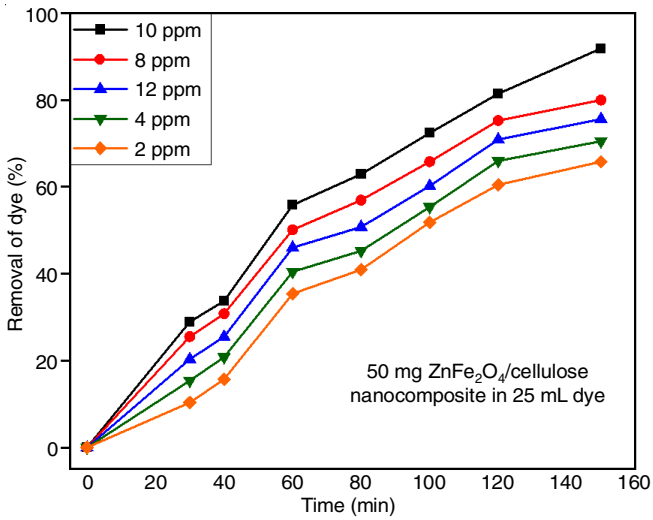

Fig. 9. Removal percentage of crystal violet dye

$$ZnFe_2O_4\text{-cellulose nanocomposites} + h\nu \longrightarrow e^-_{CB} + h^+_{VB}$$

$$e^-_{CB} + O_2 \longrightarrow O_2^{\bullet -}$$

$$h^+_{VB} + H_2O\ (H^+ + {}^-OH) \longrightarrow H^+ + OH^{\bullet -}$$

$$O_2^{\bullet -} + H^+ \longrightarrow {}^{\bullet}HO_2$$

$$2{}^{\bullet}HO_2 \longrightarrow H_2O_2 + O_2$$

$$H_2O_2 + e^- \longrightarrow OH^{\bullet} + OH^-$$

$$R\ (dye) + OH^{\bullet} \longrightarrow R^{\bullet} + H_2O$$

$$R + h^+_{VB} \longrightarrow R^{+\bullet} \longrightarrow \text{Removal product}$$

Kinetic adsorption models: The rate of projection at which crystal violet dye can be removed from an aqueous solution is necessary while designing the adsorption process. This can be studied by pseudo-first-order and pseudo-second-order. Table-1 shows the parameter of the kinetic models obtained from linear fit of the experimental data.

Pseudo-first order kinetic model: Eqn. 4 provides the pseudo-first-order kinetic model [30]:

$$\log(q_e - q_t) = \log q_e - \frac{k_1}{2.303}t \qquad (4)$$

where the amounts of dye adsorbed are q_e and q_t (μg/g) at time 't' (min^{-1}), the pseudo-first order rate constant is represented by k_1 (min^{-1}) and t is time. When log (q_e–q_t) was plotted against t, a straight line (figure not shown) showing the validity of eqn. 4 was obtained.

TABLE-1

Pseudo-first order kinetic model		
Adsorbent	K_1 (g/mg/min^{-1})	R^2
$ZnFe_2O_4$-cellulose nanocomposite	-4.666	0.86
Pseudo-second order kinetic model		
K_2 (g/mg/min^{-1})		R^2
0.1301		0.99

Pseudo-second order kinetic model: Ho & McKay [31] provided the pseudo-second-order kinetic model in linear form given by eqn. 5.

$$\frac{t}{q_t} = \frac{1}{k_2 q_e^2} + \frac{t}{q_e} \qquad (5)$$

where k_2 (g/mg/min^{-1}) is rate constant. When t/q_t is plotted against t, a straight line (figure not shown) is obtained.

The kinetic analysis revealed that the degradation of crystal violet dye proceeded in a pseudo-second-order process.

Adsorption isotherm: The interaction of the adsorbent and adsorbate, quantified the highest capacity of adsorption were graphically plotted from the experimental data and explained through different isotherms of adsorption.

Langmuir adsorption isotherm: The graph of q_e against C_e gives an excellent linearity (Fig. 10a) at different times with higher R^2 values (0.99), which is closer to 1. This graph demonstrated the appropriate and accurate prediction model present in adsorption data. The validity of the Langmuir model can be evaluated using Langmuir parameters from Table-2, where the slope and intercept of the plot, q_m and b were accomplished respectively. Eqn. 6 [32] was used to represent Langmuir adsorption, where the q_m represents the maximum adsorption per unit mass at monolayer coverage of the absorbent, b is constant, q_e and C_e is the solid and equilibrium liquid phase adsorbate concentration.

$$\frac{1}{q_e} = \frac{1}{q_m b C_e} + \frac{1}{q_m} \qquad (6)$$

Freundlich adsorption isotherm: Freundlich equation is represented by eqn. 7 [32].

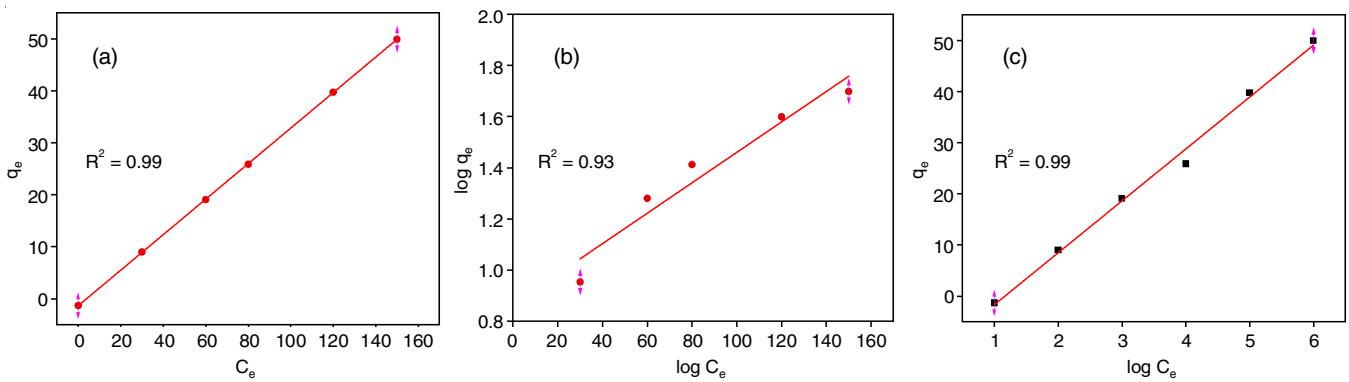

Fig. 10. Verification of (a) Langmuir, (b) Freundlich, (c) Temkin adsorption isotherms for the crystal violet dye removal by $ZnFe_2O_4$-cellulose nanocomposites

TABLE-2
PARAMETER OF VARIOUS ADSORPTION ISOTHERMS FOR ADSORPTION OF $ZnFe_2O_4$-CELLULOSE NANOCOMPOSITES

Langmuir adsorption isotherm	q_m	b	R^2
	840.747	0.93	0.99
Freundlich adsorption isotherm	K_f (mg/g)	1/n	R^2
	7.33	0.005	0.93
Temkin adsorption isotherm	B_t	K_t	R^2
	10.144	0.3124	0.99

$$\log q_e = \log K_f + \frac{1}{n}\log C_e \quad (7)$$

A straight line is obtained (Fig. 10b) showing the validity of isotherm where log q_e is plotted against log C_e and Freundlich parameters can be evaluated as shown in Table-2.

Temkin adsorption isotherm: Temkin adsorption isotherm is represented by eqn. 8 [33]. In this eq., b is represented as Temkin constant (J/mol).

$$q_e = b \ln A\, C_e \quad (8)$$

A straight line is obtained when q_e was plotted against log C_e as shown in Fig. 10c. Using this plot, the constant of the equation was calculated and shown in Table-2.

Effect of temperature: Fig. 11 represents the result of the removal of crystal violet dye by $ZnFe_2O_4$-cellulose nanocomposite at three different temperatures 308, 318 and 328 K. From the experimental data, it is observed that as the temperature increased from 308 to 328 K a reduction of crystal violet dye occurred on the nanocomposite surface. This adsorption trend suggested that crystal violet adsorption on $ZnFe_2O_4$-cellulose nanocomposite was exothermic. At the higher temperature, due to the breakdown of the weak binding interactions in between crystal violet dye and the adsorbent surface, crystal violet dye molecules may have desorbed from the surface to aqueous solution of crystal violet dye molecules and adsorption sites [27].

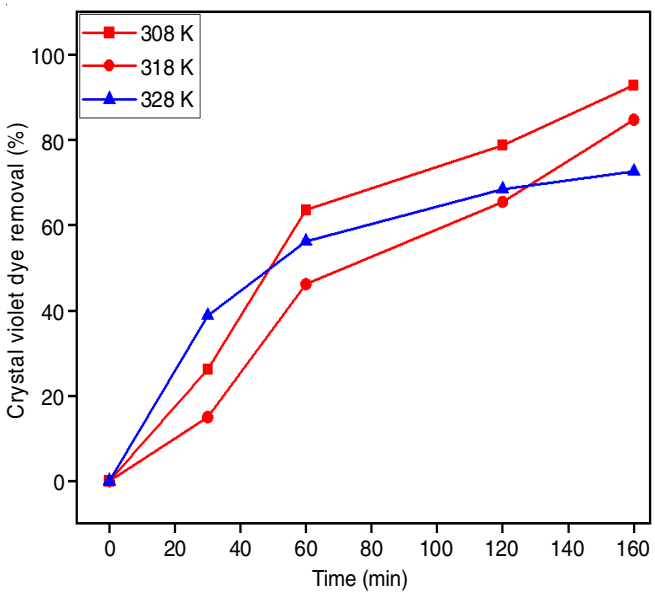

Fig. 11. Effect of temperature on removal percentage of crystal violet dye at fixed concentration

Thermodynamic studies: The adsorption nature on to $ZnFe_2O_4$-cellulose nanocomposite towards the crystal violet dye can be determined by calculating the change free energy (ΔG^o), enthalpy change (ΔH^o), entropy change (ΔS^o) and energy of activation (E_a). The thermodynamic parameter was calculated by using eqn. 9 [27].

$$\Delta G^o = -RT \ln (K_L) \quad (9)$$

where K_L = the Langmuir equilibrium constant, R = gas constant, T = temperature in Kelvin (K). The equilibrium constant K_L was calculated using eqn. 10:

$$K_L = \frac{q_e}{C_e} \quad (10)$$

$$\Delta G^o = \Delta H^o - T\Delta S^o \quad (11)$$

From eqns. 9-11, we get the below equation:

$$\ln(K_L) = \frac{\Delta S^o}{R} - \frac{\Delta H^o}{RT} \quad (12)$$

A line can be drawn by plotting ln K_L *versus* 1/T. (Fig. 12) is obtained from which ΔH^o and ΔS^o was calculated and is given in Table-3.

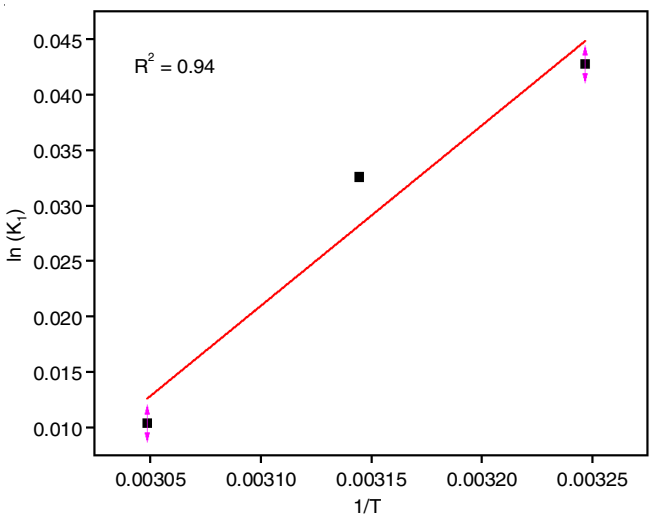

Fig. 12. Verification of eqn. 12

TABLE-3
THERMODYNAMIC PARAMETER FOR ADSORPTION OF $ZnFe_2O_4$-CELLULOSE NANOCOMPOSITES

Temp. (K)	C_e (mg/L)	K_L	ΔG^o (KJ/mol)	ΔS^o (J/mol)	ΔH^o (KJ/mol)
308	1.4	30.71	-2589.2	4.93	-1666.9
318	0.6	783.3			
328	1.8	227.7			

The negative Gibb's free energy value suggesting that the adsorption process is spontaneous in nature. In same way, the negative value of ΔH^o shows the exothermic nature of adsorption of crystal violet dye and the positive entropy change ΔS^o show that good affinity of $ZnFe_2O_4$-cellulose nanocomposites for crystal violet dye and increasing randomness of composites at the interface for solid-solution during adsorption.

TABLE-4
COMPARATIVE EVALUATION OF $ZnFe_2O_4$/CELLULOSE NANOCOMPOSITES ADSORPTION EFFICIENCY WITH RESPECT TO OTHER COMMON ADSORBENTS USED FOR CRYSTAL VIOLET DYE ADSORPTION

Adsorbent	Dose of adsorbents (g/L)	pH	Q_{max} (mg/g^{-1})	Temp. (°C)	Efficacy (%)	Ref.
$ZnFe_2O_4$/cellulose nanocomposites	0.05	6.0	840	25	92	This work
Magnetize polypeptidylated-Hb	2.00	9.0	14.8	25		[34]
MgO NPs@F	0.30	7.0	142.17	25	90	[35]
Anatolian black pine	10.00	6.9	12.36	25	NA	[36]
Titanate nanotubes	3.00	6.8	8.36	25	75	[37]
Fe_3O_4/SiO_2	0.35	6.0	16.37	25	NA	[38]

NA = Not mentioned in reference paper

Recycling studies: The recycle efficiency of synthesized $ZnFe_2O_4$-cellulose nanocomposites is represented in Fig. 13. The reusability or regeneration of adsorbent is an important aspect to evaluate the purification of contaminated water. As a result, the spot adsorbents are able to regain their original state for use in the future and their capacity for adsorption. If the adsorbents could be recycled and used again without losing their effectiveness as an adsorbent for crystal violet dye, it would be quite affordable. While reusing the adsorbents ($ZnFe_2O_4$-cellulose nanocomposites) the used adsorbent was first washed with distilled water and then with HCl to remove the impurities and then filtered with Whatman filter paper and dried for 2-3 h. After that the dried adsorbent was reused with freshly prepared dye concentration (10 ppm). When the regenerated $ZnFe_2O_4$-cellulose nanocomposite was used as an adsorbent the 90% of removal of crystal violet dye was observed at pH 6 by employing 50 mg of adsorbent in 25 mL of crystal violet dye solution after 160 min. However, removal efficiency has diminished, suggesting that at different times during adsorption and desorption, the surface activity decreases and that this in turn reduces the effectiveness of adsorption.

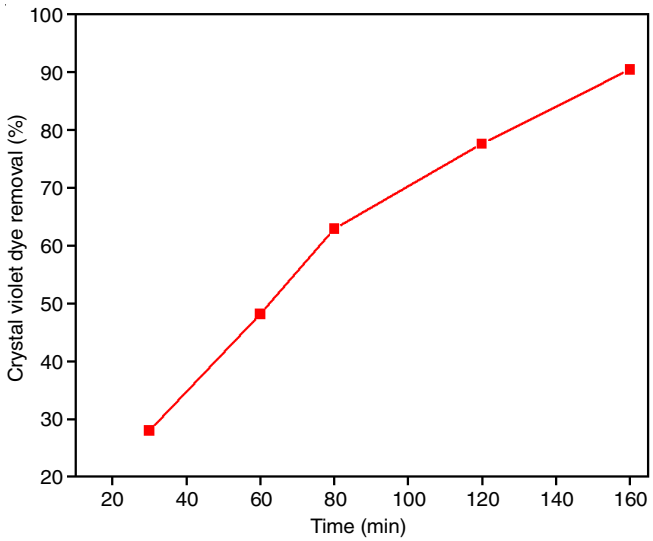

Fig. 13. Crystal violet dye adsorption and desorption on $ZnFe_2O_4$-cellulose nanocomposites at different periods

Comparative studies: Several studies on crystal violet dye adsorption utilizing various materials were reported in the literature. However, $ZnFe_2O_4$/cellulose nanocomposites were found to have the highest adsorption removal capacity for crystal violet dye (Table-4). Furthermore, $ZnFe_2O_4$ nanoparticles maximum uptake capacity increased significantly after treating with cellulose, suggesting that cellulose treatment may be a useful approach to improve crystal violet dye adsorption performance. Ultimately, the $ZnFe_2O_4$/cellulose nanocomposites developed in this study is a potential as well as cost-effective option for removal for the crystal violet dye from wastewaters.

Conclusion

$ZnFe_2O_4$-cellulose nanocomposite was prepared by using the natural polymer and characterized by X-ray diffraction, FTIR, FESEM and EDS techniques. The photocatalytic removal of crystal violet dye under solar radiation with the consideration of the pH of solution, dose of catalyst and dye concentration with the $ZnFe_2O_4$-cellulose nanocomposites was taken into consideration. The maximum 92% of dye removal can be seen at pH 6. The kinetic study of adsorption indicates that crystal violet dye adsorption on $ZnFe_2O_4$-cellulose nanocomposites is a fast process. Also, kinetic study of adsorption reveals that the experimental data of pseudo-second-order is more appropriate. The various isotherm models were used for the quantitative interpretation of adsorbate with adsorbent. The Langmuir adsorption isotherm parameter was evaluated as the best fit for the equilibrium adsorption data. The thermodynamic studies reflect that the adsorption process is exothermic and spontaneous. The maximum monolayer adsorption capacity of 50 mg $ZnFe_2O_4$-cellulose nanocomposite at 160 min indicates the possible application of $ZnFe_2O_4$-cellulose nanocomposites (adsorbent) in effluent removal of cationic dye. All results and studies reflect the efficient photocatalytic behaviour of the $ZnFe_2O_4$-cellulose nanocomposite.

ACKNOWLEDGEMENTS

The authors gratefully acknowledge the support and research facilities provided by Sharda University, Greater Noida, India.

CONFLICT OF INTEREST

The authors declare that there is no conflict of interests regarding the publication of this article.

REFERENCES

1. K. Sivaranjani, S. Sivakumar and J. Dharmaraja, *Adv. Mater. Sci.*, **22**, 28 (2022); https://doi.org/10.2478/adms-2022-0006

2. M.M.A. El-Hady and S.E. Saeed, *Polymers*, **12**, 2451 (2020); https://doi.org/10.3390/polym12112451
3. P.L. Homagai, R. Poudel, S. Poudel and A. Bhattarai, *Heliyon*, **8**, e09261 (2022); https://doi.org/10.1016/j.heliyon.2022.e09261
4. S.B. Somvanshi, S.A. Jadhav, M.V. Khedkar, P.B. Kharat, S.D. More and K.M. Jadhav, *Ceram. Int.*, **46**, 13170 (2020); https://doi.org/10.1016/j.ceramint.2020.02.091
5. E. Nakkeeran, S.J. Varjani, V. Dixit and A. Kalaiselvi, *Indian J. Exp. Biol.*, **56**, 498 (2018).
6. M. Chandrika, A.V. Ravindra, S.Y. Wang and S. Ju, *J. Mater. Sci.*, **57**, 2610 (2022); https://doi.org/10.1007/s10853-021-06701-8
7. M. Sriramulu, D. Shukla and S. Sumathi, *Mater. Res. Express*, **5**, 115404 (2018); https://doi.org/10.1088/2053-1591/aadd88
8. B. Albiss and M. Abu-dalo, *Sustainability*, **13**, 4729 (2021); https://doi.org/10.3390/su13094729
9. S. Mazhar, U.Y. Qazi, N. Nadeem, M. Zahid, A. Jalil, F. Khan, I. Ul-Hasan and I. Shahid, *Environ. Sci. Pollut. Res. Int.*, **29**, 9203 (2022); https://doi.org/10.1007/s11356-021-16181-7
10. S. Rachna, N.B. Singh and A. Agarwal, *Mater. Today Proc.*, **5**, 9148 (2018); https://doi.org/10.1016/j.matpr.2017.10.035
11. M. Gayathri, D.R. Kumar, E. Satheeshkumar, D. Manoj, A. Kumaresan, A. Arun, N. Jayaprakash and E. Sundaravadivel, *J. Mater. Sci. Mater. Electron.*, **33**, 10965 (2022); https://doi.org/10.1007/s10854-022-08076-1
12. T. Anjitha, T. Anilkumar, G. Mathew and M.T. Ramesan, *Polym. Compos.*, **40**, 2802 (2019); https://doi.org/10.1002/pc.25088
13. S. Fakhari, M. Jamzad and H. Kabiri Fard, *Green Chem. Lett. Rev.*, **12**, 19 (2019); https://doi.org/10.1080/17518253.2018.1547925
14. T. Appidi, D.B. Pemmaraju, R.A. Khan, S.B. Alvi, R. Srivastava, M. Pal, N. Khan and A.K. Rengan, *Nanoscale*, **12**, 2028 (2020); https://doi.org/10.1039/C9NR05211A
15. P. Karthikeyan, P. Sirajudheen, M.R. Nikitha and S. Meenakshi, *Environ. Nanotechnol. Monit. Manag.*, **14**, 100378 (2020); https://doi.org/10.1016/j.enmm.2020.100378
16. V.A. Fabiani, H. Aldila, Anggraeni and Nur'aini, *IOP Conf. Ser. Earth Environ. Sci.*, **599**, 012066 (2020); https://doi.org/10.1088/1755-1315/599/1/012066
17. R. Tholkappiyan and K. Vishista, *Int. J. Chemtech Res.*, **6**, 2834 (2014).
18. R.M. Borade, S.B. Somvanshi, S.B. Kale, R.P. Pawar and K.M. Jadhav, *Mater. Res. Express*, **7**, 016116 (2020); https://doi.org/10.1088/2053-1591/ab6c9c
19. J. Jiang, L. Ai and L.C. Li, *J. Mater. Sci.*, **44**, 1024 (2009); https://doi.org/10.1007/s10853-008-3225-6
20. K. Charradi, Z. Ahmed, M.A. BenMoussa, Z. Beji, A. Brahmia, I. Othman, M.A. Haija, R. Chtourou and S.M.A.S. Keshk, *Cellulose*, **29**, 2565 (2022); https://doi.org/10.1007/s10570-021-04334-3
21. V.L. Ranganatha, S. Pramila, G.N. Udayabhanu, B.S. Surendra and C. Mallikarjunaswamy, *J. Mater. Sci. Mater. Electron.*, **31**, 17386 (2020); https://doi.org/10.1007/s10854-020-04295-6
22. J. Lin, Z. Luo, J. Liu and P. Li, *Mater. Sci. Semicond. Process.*, **87**, 24 (2018); https://doi.org/10.1016/j.mssp.2018.07.003
23. S. Samsami, M. Mohamadizaniani, M.-H. Sarrafzadeh, E.R. Rene and M. Firoozbahr, *Process Saf. Environ. Prot.*, **143**, 138 (2020); https://doi.org/10.1016/j.psep.2020.05.034
24. H.B.Z.M. Zulfika, R. Baini and N.S.A. Zauzi, *IOP Conf. Ser. Mater. Sci. Eng.* **205**, 012026 (2017); https://doi.org/10.1088/1757-899X/205/1/012026
25. N. Neethu and T. Choudhury, *Recent Pat. Nanotechnol.*, **12**, 200 (2018); https://doi.org/10.2174/1872210512666181029155352
26. A. Nawaz, A. Khan, N. Ali, N. Ali and M. Bilal, *Environ. Technol. Innov.*, **20**, 101079 (2020); https://doi.org/10.1016/j.eti.2020.101079
27. M. Ait Haki, A. Imgharn, N. Aarab, A. Hsini, A. Essekri, M. Laabd, H. El Jazouli, M. Elamine, R. Lakhmiri and A. Albourine, *Water Sci. Technol.*, **85**, 433 (2022); https://doi.org/10.2166/wst.2021.451
28. A.S. Omer, G. A.El Naeem, A.I. Abd-Elhamid, O.O.M. Farahat, A.A. El-Bardan, H.M.A. Soliman and A.A. Nayl, *J. Mater. Res. Technol.*, **19**, 3241 (2022); https://doi.org/10.1016/j.jmrt.2022.06.045
29. M. Alshabanat, G. Alsenani and R. Almufarij, *J. Chem.*, **2013**, 1 (2013); https://doi.org/10.1155/2013/210239
30. S.H. Ghoran, M.F. Dashti, A. Maroofi, M. Shafiee, A. Zare-Hoseinabadi, F. Behzad, M. Mehrabi, A. Jangjou and K. Jamali, *Nanomedicine Res. J.*, **5**, 20 (2020); https://doi.org/10.22034/NMRJ.2020.01.003
31. Y.S. Ho and G. McKay, *Chem. Eng. J.*, **70**, 115 (1998). http://dx.doi.org/10.1016/S0923-0467(98)00076-1
32. S. Banerjee and Y.C. Sharma, *J. Environ. Manage.*, **233**, 151 (2019); https://doi.org/10.1016/j.jenvman.2018.11.107
33. K. Rachna, A. Agarwal and N.B. Singh, *Environ. Nanotechnol. Monit. Manag.*, **9**, 154 (2018); https://doi.org/10.1016/j.enmm.2018.03.001
34. M. Essandoh, R.A. Garcia, V.L. Palochik, M.R. Gayle and C. Liang, *Sep. Purif. Technol.*, **255**, 117701 (2021); https://doi.org/10.1016/j.seppur.2020.117701
35. D.T.C. Nguyen, H.H. Dang, D.-V.N. Vo, L.G. Bach, T.D. Nguyen and T.V. Tran, *J. Hazard. Mater.*, **404**, 124146 (2021); https://doi.org/10.1016/j.jhazmat.2020.124146
36. B.T. Gemici, H.U. Ozel and H.B. Ozel, *Sep. Sci. Technol.*, **55**, 406 (2020); https://doi.org/10.1080/01496395.2019.1577268
37. S. Mohanty, S. Moulick and S.K. Maji, *J. Water Proc. Eng.*, **37**, 101428 (2020); https://doi.org/10.1016/j.jwpe.2020.101428
38. S. Maleki, F. Falaki and M. Karimi, *J. Nanostruct. Chem.*, **9**, 129 (2019); https://doi.org/10.1007/s40097-019-0303-z